JOURNAL OF MATERIALS SCIENCE **38** (2003) 307–322

Crystal plasticity-based finite element analysis of deformation and fracture of polycrystalline lamellar γ-TiAl + α_2-Ti_3Al alloys

M. GRUJICIC, G. CAO, S. BATCHU
Department of Mechanical Engineering, Program in Materials Science and Engineering, Clemson University, Clemson SC 29634, USA
E-mail: mica@ces.clemson.edu

Deformation behavior of fully-lamellar polycrystalline γ-TiAl + α_2-Ti_3Al alloys has been analyzed using a finite element method. A three-dimensional rate-dependent, finite-strain, crystal-plasticity based materials constitutive model is used to represent the deformation behavior of the bulk material. The constitutive behavior of γ-TiAl/γ-TiAl lamellar interfaces and lamellae-colony boundaries, on the other hand, are modeled using a cohesive-zone formulation. The interface/boundary potentials used in this formulation are determined through the use of atomistic simulations of the interface/boundary decohesion. The constitutive relations for both the γ-TiAl + α_2-Ti_3Al bulk material and the lamellar interfaces and colony boundaries are implemented in the commercial finite element program Abaqus/Standard within which the material state is integrated using an Euler-backward implicit formulation. The results obtained show that plastic flow localizes into deformation bands even at an overall strain level of only 0.5% and that incompatibilities in plastic flow between the adjacent colonies can give rise to high levels of the hydrostatic stress and, in turn, to intercolony fracture. Furthermore, it is found that when lamellar interfaces are admitted into colonies, fracture is delayed and the materials fail in a more gradual manner.

1. Introduction

Two-phase γ-TiAl + α_2-Ti_3Al alloys with micron-scale lamellar microstructures generally exhibit a good combination of high-temperature properties such as creep resistance, microstructural stability, oxidation resistance, etc. Consequently, there has been much interest in developing these alloys as viable materials for high-temperature structural applications. However, a lack of tensile ductility and fracture toughness in these alloys at the ambient temperature is one of the major shortcomings which hampers their wide use. There are several comprehensive reviews [e.g., 1–3], that summarize the major advances in development of these alloys. It should be pointed out, however, that the main improvements in alloy properties have been realized largely in polysynthetically-twinned single-crystalline form of these materials, and that it has been quite difficult to achieve similar successes in the polycrystalline materials of this type. The latter typically fail at tensile strains less than 3% and generally have a fracture toughness level K_{IC} below 30 MPa$\sqrt{m}$. While single crystalline materials of this type possess quite attractive properties, their use is cost prohibitive. Thus, achieving a superior combination of properties in conventionally processed polycrystalline γ-TiAl + α_2-Ti_3Al alloys remains an important, though formidable, engineering challenge.

During solidification, Ti-(48–50) at.% Al alloys, which are considered in the present work, first form a disordered hexagonal-close-packed (h.c.p.) α-phase which during cooling orders into an α_2-Ti_3Al-type phase with the DO_{19} crystal structure and then transforms to (or near) completion into an ordered face-centered-tetragonal (f.c.t.) γ-TiAl phase with the $L1_0$ crystal structure. The final microstructure typically consists of colonies each containing micron-thick parallel γ-TiAl and α_2-Ti_3Al lamellae with a standard f.c.c.-h.c.p. type orientation relationship between the two phases: $\{111\}_\gamma \| (0001)_{\alpha 2}$ and $\langle 1\text{–}10]_\gamma \| \langle 11\text{–}20\rangle \alpha_2$. In addition, the γ/α_2 and γ/γ lamellar boundaries have the following crystallographic orientations: $\{111\}_\gamma \| (0001)_{\alpha 2}$ and $\{111\}_\gamma \| \{111\}_\gamma$, respectively. Under unidirectional solidification condition, the microstructure of Ti-(48–50) at.% Al can be obtained which consists of a single colony of γ-TiAl + α_2-Ti_3Al lamellae [e.g., 4]. Such alloys are referred to as having polysynthetically-twinned single crystalline microstructure.

The microstructure of polycrystalline γ-TiAl + α_2-Ti_3Al alloys can be modified using post-solidification heat treatments at different temperatures, holding times and cooling rates [e.g., 5]. The resulting microstructures are generally classified as: near-gamma, duplex, nearly lamellar, and fully lamellar. For Ti-(48–50) at.% Al alloys, fully-lamellar and duplex microstructure impart

the best combinations of mechanical properties. The fully-lamellar microstructure consists of colonies of γ-TiAl + α_2-Ti_3Al lamellae where the colony size is controlled by the holding time at the heat-treating temperature while the rate of cooling to room temperature governs the thickness of lamellae. The duplex microstructure contains in addition to the γ-TiAl and α_2-Ti_3Al lamellae, small γ-TiAl phase particles typically located at the colony boundaries. In this case, the heat-treating temperature and the holding time affects the volume fraction of the phases, while the cooling rate determines the lamellar thickness. In the present work, only fully-lamellar polycrystalline γ-TiAl + α_2-Ti_3Al alloys will be analyzed.

The mechanical response of γ-TiAl + α_2-Ti_3Al polysynthetically twinned single-crystalline alloys is highly anisotropic at the macroscopic, microscopic and crystal structure length scales [e.g., 4]. At the macroscopic length scale, properties such as flow stress, fracture stress, fracture strain, crack growth rate and others exhibit strong orientation dependence. In the γ-TiAl + α_2-Ti_3Al lamellar microstructure, γ-TiAl is the softer phase and its flow properties are highly anisotropic due to the lamellar geometry of its crystals. Shear deformation parallel to the lamellar interfaces is considerably easier (the soft mode) than that normal to them (the hard mode). In the latter case, slip in the γ-TiAl phase is constrained by the harder α_2-Ti_3Al phase [4]. Since the soft-to-hard mode slip length ratio is typically on the order of 100, the Hall-Petch effect is significant. In addition, the Hall-Petch slopes are also anisotropic, with typical values 0.273 and 0.440 MPa/$\sqrt{m}$ for the soft and the hard modes, respectively [6]. Hence, at the microscopic length-scale, materials anisotropy is caused primarily by large differences in the soft and hard mode deformation resistances within each phase and differences in the deformation resistances of the two phases. At the crystal-structure length scale, materials anisotropy is derived from differences in deformation resistance of different slip systems within the same phase. For example, $\langle a \rangle$-slip systems associated with $\langle 11\bar{2}0 \rangle$ slip directions are generally substantially softer than any of the possible $(c + a)$-slip systems in α_2-Ti_3Al. Since the latter systems are needed to achieve a general state of strain, the α_2-Ti_3Al phase can be considered as kinematically constrained in the c-direction [e.g., 7].

The anisotropic behavior of polysynthetically-twinned γ-TiAl + α_2-Ti_3Al single crystals described above is, to some extent, retained in the polycrystalline form of these materials. However, additional changes in the mechanical behavior of lamellar γ-TiAl + α_2-Ti_3Al polycrystals arises from variations in the microstructure such as: the shape, size, and volume fraction of the constituent phases. For example, fully lamellar and duplex alloys exhibit an inverse tensile elongation/fracture toughness relationship [5]. That is, while the flow behavior (yield stress, rate of strain hardening, etc.) is quite similar in the two microstructures, fully lamellar alloys have low ductility ($\sim$<3%) and relatively high fracture toughness ($K_{IC} \approx$ 22–32 MPa$\sqrt{m}$), whereas the duplex alloys have high ductilities ($\sim$5–10%) and low fracture toughness ($K_{IC} \approx$ 10–12 MPa$\sqrt{m}$) [5].

While tensile fracture strains on the order of 30% have been found in polysynthetically-twinned γ-TiAl + α_2-Ti_3Al single crystals [10], polycrystalline forms of these materials show a drastically lower tensile ductility (<3%) [7]. Such disparities in mechanical behavior of single and polycrystalline alloys have been widely reported, however the origin of this phenomenon is still not well understood. Often, it is postulated to arise from the constraints to plastic flow in a colony or grain imposed by the surrounding colonies or grains, the phenomenon, which is present only in polycrystalline materials.

The objective of the present work is to provide a suitable rationale for the aforementioned limited ductility and fracture toughness in polycrystalline γ-TiAl + α_2-Ti_3Al alloys and to help establish relationships between the microstructure (particularly the effect of γ-TiAl/γ-TiAl lamellar interfaces) and properties in these materials. Toward that end, a rate-dependent, finite strain, crystal-plasticity material constitutive model is developed, implemented into the commercial finite element package Abaqus/Standard [8] and employed to predict the global response of polycrystalline material. The approach used provides an opportunity to study the evolution of strain localization and to help reveal the contribution strain localization makes to the global mechanical response of the material. For example, due to the soft-vs. hard-mode flow-stress disparity, non-uniform deformation is likely to occur in polycrystalline γ-TiAl + α_2-Ti_3Al alloys containing randomly oriented lamellar colonies. In fact, plastic flow non-uniformity leading to strain localization near grain boundaries and three grain junctions are observed at small plastic strains even in f.c.c. metallic materials in which due to a large number of crystallographically equivalent slip systems all of the identical (initial) deformation resistance, strain localization is more difficult to develop [9, 10]. Since γ-TiAl and α_2-Ti_3Al possess slip systems of different crystallographic nature whose deformation resistances can differ substantially so that these materials can be considered kinematically constrained with respect to certain deformation modes, strain localization is more likely to occur and should occur at lower plastic strains. Strain localizations in the regions near the colony/grain boundaries and three colony/grain junctions are generally associated with large local stress concentrations and since these stresses might be precursors to material failure, understanding their evolution during deformation, their relationships to the local microstructure and their contribution to the global materials response is highly important and will be studied in the present work. A comprehensive finite element analysis of the deformation and fracture behavior of the two phase γ-TiAl + α_2-Ti_3Al alloys was conducted in a series of papers by Asaro and coworkers [7, 11, 12]. However, while the analysis of Asaro and coworkers [7, 11, 12] provided important insight into the effect of colony to colony misorientation on the local incompatibility of plastic flow and the resulting stress concentration, no provision was made for the materials fracture. To overcome this limitation, fracture along γ-TiAl/γ-TiAl lamellar interfaces and colony boundaries is allowed in the present work through the use of

a cohesive zone formulation. Also, a three-dimensional crystal-plasticity materials constitutive model recently proposed by Grujicic and Batchu [13] which incorporates kinematic constraints arising from the retention of the crystallographic nature of γ-TiAl/α_2-Ti_3Al interlamellar boundaries and the retention of the γ-TiAl vs. α_2-Ti_3Al orientation relationship is used.

The organization of the paper is as follows: A brief overview of the derivation of the constituent response of lamellar interfaces and colony boundaries and the derivation of the stiffness matrix for the corresponding interfacial elements suitable for implementation into a finite element analysis are provided in Section 2.1. The crystal plasticity model for polysynthetically-twinned γ-TiAl + α_2-Ti_3Al single crystals and its implementation into the commercial finite element package Abaqus/Standard are reviewed in Section 2.2. An outline of the boundary value problem analyzed in the present work through the use of finite element method is presented in Section 2.3. The main computational results are shown and discussed in Section 3. A summary of the key conclusions resulted from the present work is presented in Section 4.

2. Computational procedure

2.1. γ-TiAl/γ-TiAl lamellar-interface and colony-boundary constitutive relations

To comply with the experimental observations [e.g., 5], fracture is allowed to occur along the γ-TiAl/γ-TiAl lamellar interfaces and colony boundaries. Toward this end, the mechanical constitutive response of the γ-TiAl/γ-TiAl lamellar interfaces and the boundaries between γ-TiAl + α_2-Ti_3Al lamellar colonies is modeled using the cohesive zone framework originally introduced by Needleman [14]. The cohesive zone is assumed to have a negligible thickness when compared to other characteristic lengths of the problem, such as the lamellae thickness, typical lengths associated with the gradient of the fields, etc. The mechanical behavior of the cohesive zone is characterized by a traction-displacement relation which is introduced through the definition of an interface potential, Φ. Stable equilibrium for an interface boundary corresponds to a perfectly bonded configuration, where the potential has a minimum and all tractions vanish. For any other configuration, the value of the potential is taken to depend only on the displacement jump across the interface. In general, an interface displacement jump is expressed in terms of its normal component, U_n, and two tangential components, U_t and U_b. Differentiation of the interface potential function Φ with respect to U_n, U_t and U_b yields, respectively, a normal and two tangential components of the traction per unit interface area in the deformed configuration. Thus the interface constitutive relations are fully defined by specifying the form for the interface potential function. In the present work, the approach based on the use of Molecular Statics method recently proposed by Grujicic and Lai [15] is used to determine the interface potential for the γ-TiAl/γ-TiAl lamellar interfaces and colony boundaries. A brief overview of this approach is given below.

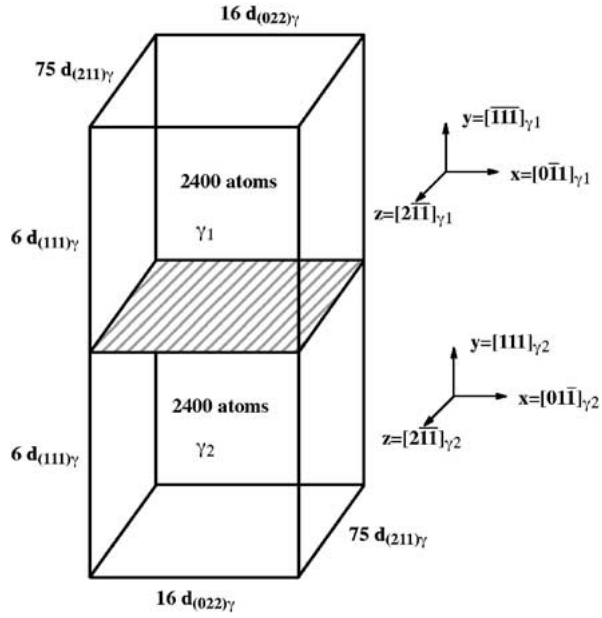

Figure 1 Schematic representation of the γ-TiAl/γ-TiAl ($\gamma 1/\gamma 2$) bicrystal used for determination of the $(111)_{\gamma 1}/(111)_{\gamma 2}$ lamellar interfacial potential.

To determine the potential function for a particular γ-TiAl/γ-TiAl lamellar interface or colony boundary, a γ-TiAl/γ-TiAl atomistic bicrystal is first constructed from two appropriately orientated single crystals and with the appropriate orientation of the interface/boundary separating the single crystals. An example of the γ-TiAl/γ-TiAl atomistic bicrystal is given in Fig. 1. The single crystals edge lengths are expressed in terms of the number of interplanar spacings $d_{(uvw)}$ of the corresponding (uvw) planes, where (uvw) are the plane Miller indices. The atomic interactions are accounted for through the use of the Embedded Atom Method (EAM) interatomic potential [16]. Interatomic potentials, which account for the atomic interactions in a crystal, are the required input for any atomistic simulation study and therefore their reliability and accuracy are very critical for the atomistic simulations to faithfully represent the materials behavior. In contrast to the traditional pair potentials, the EAM interatomic potentials take into account, in an implicit way, the many-body effects and have therefore been proven more reliable in representing the atomic interactions in metals [e.g., 17]. As mentioned earlier, γ-TiAl has an $L1_0$-type ordered crystal structure, and hence the interatomic potential functions must account for the Ti-Ti, Al-Al and Ti-Al interactions and for the fact that the two atomic species (Ti and Al) reside on separate crystal sublattices. Farkas [18] recently developed the EAM-type interatomic potentials for γ-TiAl and showed that a reasonable agreement can be obtained between the model predictions and the experimentally measured properties of this phase. In addition, this potential has been extensively tested and validated in our previous work, Grujicic and Dang [19, 20], Grujicic and Lai [21] and Grujicic and Zhang [22, 23], and hence is used in the present study.

Prior to constructing a simulation bicrystal, the equilibrium lattice parameters of γ-TiAl at 0 K are determined by carrying out the Molecular-statics type

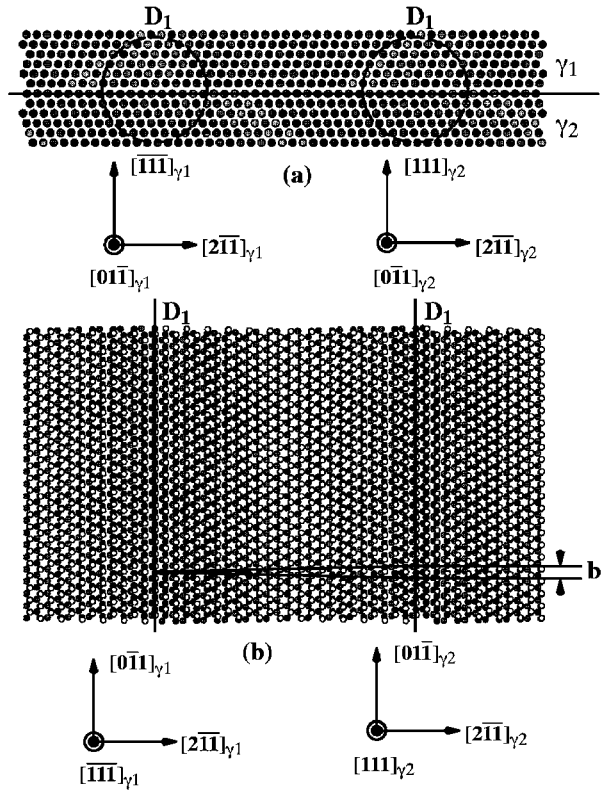

Figure 2 Equilibrium configuration of the $[\bar{1}\bar{1}\bar{1}]_{\gamma 1}//[111]_{\gamma 2}$ lamellar interface. Atomic positions projected onto: (a) the $[01\bar{1}]_{\gamma 1}//[0\bar{1}1]_{\gamma 2}$ plane; and (b) the $[\bar{1}\bar{1}\bar{1}]_{\gamma 1}//[111]_{\gamma 2}$ interface plane. Interfacial dislocations are marked as D_1 while the magnitude of their Burger's vector is denoted as b.

potential energy minimization through the use of the Conjugate Gradient Method [24]. The following lattice parameters are obtained for γ-TiAl: $a_\gamma = 3.944$ Å and $c_\gamma = 4.010$ Å, resulting in the c_γ/a_γ ratio of 1.05 which is in fair agreement with its experimental counterpart $c_\gamma/a_\gamma = 1.03$ [25].

Before the appropriate γ-TiAl/$\gamma-$TiAl interface potentials can be evaluated, the reference stress-free equilibrium structure of the interface must be determined. The equilibrium interface structure at 0 K is determined in each case by minimizing the potential energy of the corresponding bicrystals using the Conjugate Gradient Method under the flexible periodic boundary conditions in two mutually orthogonal directions parallel with the plane of interface and the free surface boundary conditions in the direction normal to the interface. The use of the free surface boundary conditions allows the spacing of the planes parallel to and near the interface to adjust to differences in the atomic environment. An example of the equilibrium atomistic configuration for the γ-TiAl/γ-TiAl lamellar interface is shown in Fig. 2a and b. Two views of the interface structure are given in Fig. 2a and b. In Fig. 2a, atoms of the two crystals are projected on a plane normal to the interface. In Fig. 2b, on the other hand, the atoms are projected on the plane of the interface. As indicated in Fig. 2a and b, the interface structure is dominated by an array of parallel screw dislocations marked $D1$. The characteristics of the array $D1$ are given in Table I.

The interface potential functions for each of the lamellar interfaces and colony boundaries analyzed are determined by first rigidly displacing the two single crystals from the equilibrium configuration of the bicrystal such as the one shown in Fig. 2a and b, in the normal n and tangential t and b directions by different amounts. These three displacements are respectively designated as: U_n, U_t and U_b. The potential energy of the perturbed bicrystals is next minimized under the constraint that the average displacements of the atoms in the interface planes in each of the two single crystals remain equal to the rigid displacements U_n, U_t and U_b. The difference between the energies of the bicrystal in the displaced configuration and in the stress-free equilibrium configuration expressed per unit area of the interface is then defined as the value of the interface potential Φ at the given values of U_n, U_t and U_b.

TABLE I Parameters characterizing dislocation structure in the γ-TiAl/γ-TiAl lamellar interface shown in Fig. 2a and b

Parameter	Value
Line direction l	$[0\bar{1}1]_\gamma$
Burger's vector b	$1/2\ a_\gamma c_\gamma/\sqrt{a_\gamma^2 + c_\gamma^2}[0\bar{1}1]_\gamma$
Dislocation spacing λ	$25a_\gamma\sqrt{\left(a_\gamma^2 + 2c_\gamma^2\right)/\left(a_\gamma^2 + c_\gamma^2\right)}$

The calculation results of the interface potential Φ for the γ-TiAl/γ-TiAl lamellar interface, whose equilibrium atomic configuration is shown in Fig. 2a and b, are shown in Fig. 3a and b. The variation of Φ with the normal interface displacement U_n at various values of the tangential displacement U_t and $U_b = 0$ is given in Fig. 3a. The variation of Φ with the tangential displacement U_t at various values of the tangential displacement U_b and the zero value of normal displacement U_n is shown in Fig. 3b. The tangential direction b is chosen to coincide with the line vector ($[0\bar{1}1]_{\gamma 1} \| [01\bar{1}]_{\gamma 2}$) of the interface dislocations while the tangential vector $t([2\bar{1}\bar{1}]_{\gamma 1} \| [2\bar{1}\bar{1}]_{\gamma 2})$ is taken to be normal to it. Based on the analysis of over 50 γ-TiAl/γ-TiAl interfaces (the results for only one given here for brevity), the overall behavior of the computed-interface potentials with the variation in the three displacements can be summarized as following:

(a) For the pure normal decohesion process where $U_t = U_b = 0$, the interface potential increases monotonically with the normal displacement U_n and asymptotically approaches a value defined as the work of decohesion, Φ_{dec}.

(b) At non-zero values of the tangential displacements, (for example for $U_t = 10$ nm and $U_b = 0$ as in Fig. 3a), the interface potential first decreases and then increases with the normal displacement U_n.

(c) The shear behavior of the interface is periodic with the periodic length governed by the spacing of the interfacial dislocations. For example, the periodic length for Φ in Fig. 3b is equal to the spacing l of the interfacial dislocations $D1$ in Fig. 2a and b.

(d) The pure shear behavior is unstable in some cases (not shown for brevity) since perturbations in the normal U_n or in the orthogonal shear displacements can give rise to a reduction in the potential.

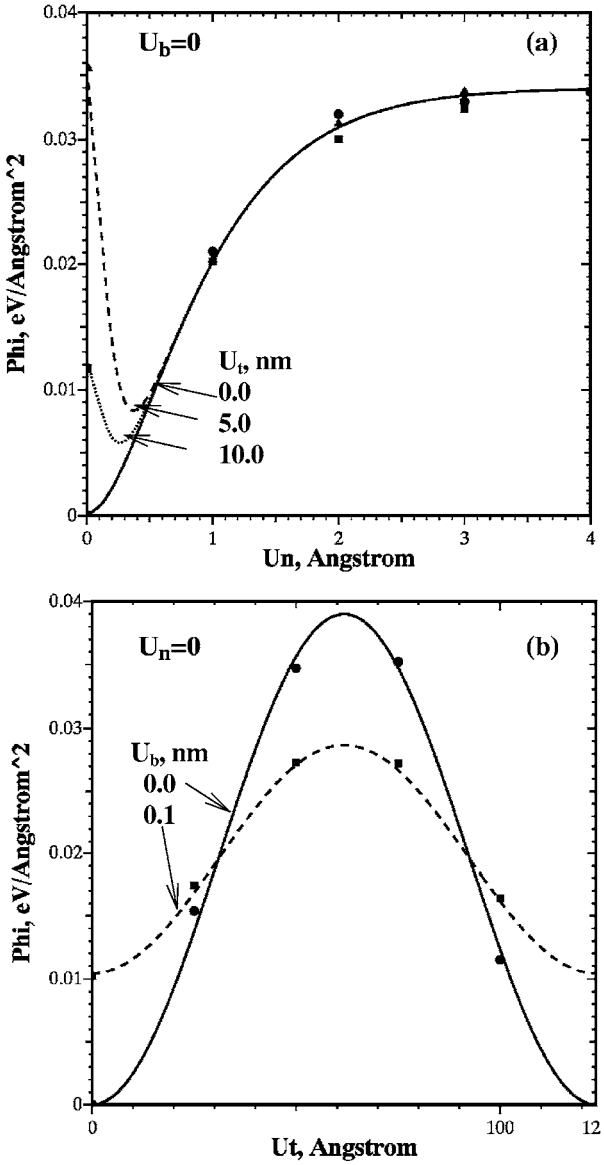

Figure 3 Variation of the interface potential for the $(111)_{\gamma 1}//(111)_{\gamma 2}$ lamellar interface with the normal displacement U_n in the $[\bar{1}\bar{1}\bar{1}]_{\gamma 1}//[111]_{\gamma 2}$ direction and tangential displacements U_t and U_b in the $[01\bar{1}]_{\gamma 1}//[0\bar{1}1]_{\gamma 2}$ and $[2\bar{1}\bar{1}]_{\gamma 1}//[2\bar{1}\bar{1}]_{\gamma 2}$ directions, respectively.

(e) In some cases (not shown for brevity) the shear behavior is not symmetric which has been shown to be related to the non-planar step + ledge character of the interface [15].

Since every γ-TiAl/γ-TiAl lamellar interfaces and colony-boundary appearing in the finite element representation of the microstructure in polycrystalline γ-TiAl + α_2-Ti_3Al materials will be analyzed using the cohesive zone approach, it is useful to express the interface/boundary potential for all of them using the same functional form. The fact that pure shear is unstable in some cases, rules out the use of the interface potential function proposed by both Needleman [14] and Socrate [26]. Furthermore, due to the nonsymmetrical character of the interface shear, the universal function for ideal shear proposed by Bozzolo *et al.* [27] could also not be used. After analyzing a number of combinations of the aforementioned interface potential functions, the following function is found to best mimic the overall relationship between Φ and U_n, U_t and U_b for all γ-TiAl/γ-TiAl lamellar interfaces and colony boundaries analyzed:

$$\Phi = \sigma_{\max}\delta_n\left[e - \left(\frac{U_n}{\delta_n}+1\right)\exp^{[(U_n/\delta_n)+1]}\right] + \frac{1}{2}\alpha_0\left(\frac{6U_n}{\delta_n}+1\right)\exp^{(6U_n/\delta_n)} \times\left\{\alpha_1 + \left[\alpha_2 \sin\frac{4\pi(U_s-2)}{\lambda_s} + \cos\left(\frac{2\pi U_s}{\lambda_s}+\alpha_3\right) + \alpha_4\right]\left(\alpha_5 + \cos\frac{2\pi U_b}{\lambda_b}\right)\right\} \quad (1)$$

Table II gives a summary of the parameters appearing in Equation 1 for the lamellar interfaces whose atomistic structure is displayed in Fig. 2a and b and for one colony boundary (atomistic structure not shown for brevity).

It should be noted that several parameters appearing in Equation 1 have a particular physical meaning:

- $\sigma_{s\,\max}$ is the normal interface strength associated with the pure normal decohesion processes ($U_b = U_t = 0$) and corresponds to the normal traction at the normal interfacial displacement $U_n = \delta_n$.
- λ_b and λ_t are the periodic lengths for pure shear in the two shear directions b and t, respectively and are related to the spacing of the corresponding interfacial dislocations.
- The shear interface strengths in the two directions, $\tau_{\max,\,b}$ and $\tau_{\max,t}$, correspond to two pure shear modes of interface decohesion and occur at $U_b = 0.25\lambda_b$, $U_n = U_b = 0$ and $U_t = 0.25\lambda_t$, $U_n = U_b = 0$, respectively.

The difference between the interface potential in the limit $U_n \to \infty$, and its equilibrium magnitude at $U_n = U_b = U_t = 0$, is generally termed the work of decohesion and is taken to be in the range of 1–10 J/m^2.

TABLE II Decohesion potential parameters for one γ-TiAl/γ-TiAl lamellar interface and one colony boundary

	Interface type	
Parameter	$(111)_{\gamma 1}/(111)_{\gamma 2}$ Lamellar boundary	$(001)_{\gamma 1}/(0\bar{1}1)_{\gamma 2}$ Colony boundary
n-Direction	$[\bar{1}\bar{1}\bar{1}]_{\gamma 1}/[111]_{\gamma 2}$	$(001)_{\gamma 1}/(0\bar{1}1)_{\gamma 2}$
t-Direction	$[\bar{1}\bar{1}\bar{1}]_{\gamma 1}/[111]_{\gamma 2}$	$(\bar{1}\bar{1}0)_{\gamma 1}/(\bar{1}\bar{1}\bar{1})_{\gamma 2}$
b-Direction	$[\bar{1}\bar{1}\bar{1}]_{\gamma 1}/[111]_{\gamma 2}$	$(\bar{1}\bar{1}0)_{\gamma 1}/(2\bar{1}\bar{1})_{\gamma 2}$
δ_n, nm	0.05	0.05
λ_t, nm	12.35	3.67
λ_b, nm	0.578	1.07
α_1	−0.039	−0.145
α_2	−1	0.42
α_3	0	−0.31
α_4	0	−3.42
α_5	0	1.17
α_0	0	−5.02
$\sigma_{\max}$ (GPa)	2.01	1.21
$\tau_{\max,t}$ (GPa)	0.160	12.7
$\tau_{\max,b}$ (GPa)	1.65	0.73
$\Phi(U_n \to \infty)$ (J/m^2)	0.561	0.374

The results obtained such as the one given in Table II are generally consistent with this range. The normal interface strength σ_{max} is generally assumed to be 0.01 to 0.02 times the material Young's modulus, which yields 1.6–3.2 GPa for the γ-TiAl phase. The normal interface strength data given in Table II are consistent with this range of values. As for the shear interface strength, it is generally assumed to be a relatively small fraction of σ_{max}. An examination of the results given in Table II, shows that this is true for $\tau_{max,t}$ for the $(111)_{\gamma 1}/(111)_{\gamma 2}$ lamellar boundary but not for the $(001)_{\gamma 1}/(0\bar{1}1)_{\gamma 2}$ colony boundary. In addition, the shear resistances in the b and t directions are quite different from each other and, as in the case of the $(001)_{\gamma 1}/(0\bar{1}1)_{\gamma 2}$ colony boundary, the shear resistance $\tau_{max,t}$ can be significantly larger than σ_{max}. This finding is a direct consequence of the non-planar interface morphology, which consists of steps and ledges aligned in the b direction. Similarly, the presence of a single array of dislocations in the case of γ-TiAl/γ-TiAl lamellar interface causes the two shear resistances, $\tau_{max,t}$ and $\tau_{max,b}$ to differ by more than an order of magnitude.

Once the γ-TiAl/γ-TiAl interface/boundaries potentials are derived, they are used to construct (continuum) interfacial elements, which are suitable for a finite element analysis. A brief description of the derivation of the stiffness matrix of continuum interfacial elements is given in Appendix.

2.2. Materials constitutive model for polysynthetically-twinned γ-TiAl + α_2 Ti_3Al single crystals

The deformation behavior of polysynthetically-twinned γ-TiAl + α_2-Ti_3Al single crystals has been recently modeled by Grujicic and Batchu [13] using a rate-dependent, isothermal, elastic-viscoplastic, finite-strain, crystal-plasticity formulation. The continuum mechanics foundation for this model can be traced to the work of Teodosiu [28], Hill and Rice [29], Mandel [30], Teodosiu and Sidoroff [9], Asaro and Rice [10] and Asaro [31]. The work of Kocks *et al*. [32], Frost and Ashby [33], and Argon [34], on the other hand, provides a more materials science viewpoint of the subject matter.

It is well established [e.g., 4] that plastic deformation in polysynthetically-twinned γ-TiAl + α_2-Ti_3Al single crystals parallel to the interlamellar γ-TiAl/α_2-Ti_3Al interfaces is substantially easier (the soft mode) than deformation normal to these interfaces (the hard mode). Therefore, the two modes of deformation are considered separately.

In γ-TiAl lamellae, plastic deformation on planes parallel to the $(111)_\gamma \| (0001)_{\alpha 2}$ interfaces is controlled both by the $\langle 1\bar{1}0]\langle 111)$ and the $\langle 10\bar{1}](111)$ slip systems. Grujicic and Batchu [13] found that slip resistances and strain hardening characteristics differ in these two slip systems in γ-TiAl single crystals. In polysynthetically-twinned γ-TiAl + α_2-Ti_3Al, each γ-TiAl lamella consists of multiple crystallographically-equivalent domains of this phase. The domains differ from each other with respect to along which of the six $\langle 11\bar{2}0\rangle$ directions of the α_2-Ti_3Al phase is $\langle 10\bar{1}]$ direction of the γ-TiAl aligned in the $(111)_\gamma \| (0001)_{\alpha 2}$ lamellar interface. Since the probability for formation of each domain is the same, the effective slip properties of γ-TiAl lamella are assumed to be essentially equal in all close-packed directions in the (111) plane parallel to the lamellar interface. Since there are twice as many $\langle 10\bar{1}]$ directions than $\langle 1\bar{1}0]$ directions in a (111) plane of the γ-TiAl phase, and the probability for occurrence of each domain in a γ-TiAl lamella is essentially the same, Grujicic and Batchu [13] defined the effective properties for the soft-mode deformation of the γ-TiAl lamellae as a weighted average of those associated with $\langle 1\bar{1}0](111)$ (weighting factor = 1/3) and $\langle 10\bar{1}](111)$ (weighting factor = 2/3) slip systems in γ-TiAl single crystals.

For the soft-mode plastic deformation of γ-TiAl lamellae, which involves slip in the close-packed directions parallel to the interlamellar boundaries but on planes inclined with respect to these boundaries. Grujicic and Batchu [13] found that its deformation resistance is somewhat higher than that associated with slip on planes parallel to the lamellar interfaces.

The contribution of plastic deformation of the α_2-Ti_3Al lamellae in a direction parallel to the $(111)_\gamma \| (0001)_{\alpha 2}$ lamellar boundaries is neglected by Grujicic and Batchu [13] for the following reasons: (a) The soft-mode plastic deformation is expected to be dominated by the softer (γ-TiAl) phase; and (b) since the volume fraction of the α_2-Ti_3Al lamellae is typically an order of magnitude smaller than that of the γ-TiAl lamellae, the role of α_2-Ti_3Al in the soft-mode deformation is expected to be minimal.

The situation is quite different for the hard-mode of plastic deformation, i.e. for plastic deformation, which includes a component normal to the $(111)_\gamma \| (0001)_{\alpha 2}$ lamellar interfaces. In this case slip is controlled by the phase which exerts more resistance toward this mode of plastic deformation, the α_2-Ti_3Al phase. As established experimentally [35], the only slip system in α_2-Ti_3Al which gives rise to this type of plastic deformation is the $\{11\bar{2}1\}\langle 11\bar{2}6\rangle$-$\langle c+a\rangle$ slip system. Hence, this slip system is expected to control the hard-mode of plastic deformation in polysynthetically-twinned γ-TiAl + α_2-Ti_3Al single crystals. However, since the volume fraction of α_2-Ti_3Al is typically less than one tenth of that of γ-TiAl, and γ-TiAl appears as multiple lamellae, limited hard-mode plastic deformation in γ-TiAl is allowed. This possibility is incorporated implicitly by Grujicic and Batchu [13] by allowing the $\{11\bar{2}1\}\langle 11\bar{2}6\rangle$ slip systems in α_2-Ti_3Al lamellae of polysynthetically-twinned γ-TiAl + α_2-Ti_3Al to have a lower deformation resistance relative to that in α_2-Ti_3Al single crystals.

To summarize, the soft-mode plastic deformation behavior of polysynthetically-twinned γ-TiAl + α_2-Ti_3Al single crystals is assumed to be controlled by the $\{111\}\langle 1\bar{1}0\rangle$ slip systems of γ-TiAl with the slip direction parallel with the lamellar interfaces, while the hard mode plastic deformation is taken to be controlled by the $\{11\bar{2}1\}\langle 11\bar{2}6\rangle$ slip of α_2-Ti_3Al. A detailed analysis of deformation and strain-hardening behavior of polysynthetically-twinned γ-TiAl + α_2-Ti_3Al single crystals is given in reference [13].

The materials constitutive model developed by Grujicic and Batchu [13] assumes that each material point contains a single material which is obtained by proper homogenization of the two phases: γ-TiAl and α_2-Ti_3Al. The (initial) reference configuration in this material is taken to consist of a perfect stress-free crystal lattice and the embedded material. The position of each material point in the reference configuration is given by its position vector X. In the current configuration, each material point is described by its position vector, x, and hence, mapping of the reference configuration into the current configuration is described by the deformation gradient, $F = \partial x/\partial X$. In order to reach the current configuration, the reference configuration must be deformed both elastically and plastically and, hence, the total deformation gradient can be multiplicatively decomposed into its elastic, F^e, and plastic, F^P, parts as $F = F^e F^p$. In other words, the deformation of a single-crystal material point is considered to be the result of two independent atomic-scale processes: (i) an elastic distortion of the crystal lattice corresponding to the stretching of atomic bonds and; (ii) a plastic deformation which is associated with atomic plane slippage which leaves the crystal lattice undisturbed. While twinning is a potential inelastic deformation mechanism at lower temperatures and higher strain rates, only slip on well defined crystallographic planes in low-index crystallographic directions is considered.

The constitutive model of Grujicic and Batchu [13] is based on the following governing variables: (i) The Cauchy stress, T; (ii) The deformation gradient, F; (iii) Crystal slip systems, labeled by integers α. Each slip system is specified by a unit slip-plane normal n_0^α, and a unit vector m_0^α aligned in the slip direction, both defined in the reference configuration; (iv) The plastic deformation gradient, F^p, with $\det F^p = 1$ (plastic deformation by slip does not give rise to a volume change) and; (v) The slip system deformation resistance $s^\alpha > 0$ which has the units of stress.

Based on the aforementioned multiplicative decomposition of the deformation gradient, the elastic deformation gradient F^e which describes the elastic distortions and rigid-body rotations of the crystal lattice, can be defined by:

$$F^e \equiv F F^{p-1}, \quad \det F^e > 0. \tag{2}$$

The plastic deformation gradient, F^p, on the other hand, accounts for the cumulative effect of shearing on all slip systems in the crystal.

Since elastic stretches in intermetallic materials such as γ-TiAl and α_2-Ti_3Al are generally small, the constitutive equation for stress under isothermal conditions can be defined by the linear relation:

$$T^* = C[E^e] \tag{3}$$

where C is a fourth-order anisotropic elasticity tensor, and E^e and T^* are respectively the Green elastic strain measure and the second Piola-Kirchhoff stress measure relative to the isoclinic configuration obtained after plastic shearing of the lattice as described by F^p. E^e and T^* are respectively defined as:

$$E^e \equiv (1/2)\{F^{eT} F^e - I \quad T^* \equiv (\det F^e) F^{e-1} T F^{e-T} \tag{4}$$

where I is the second order identity tensor.

The elasticity tensor C (expressed as a 6×6 square matrix with respect to the appropriate crystal-structure based Cartesian coordinate system), for the tetragonal γ-TiAl phase contains six independent non-zero components: $C_{11} = C_{22}$, C_{33}, C_{12}, $C_{13} = C_{23}$, $C_{44} = C_{55}$, and C_{66}. The hexagonal α_2-Ti_3Al phase exhibits transverse elastic isotropy and, hence, its elasticity tensor contains six different (five independent) non-zero components: $C_{11} = C_{22}$, C_{33}, C_{12}, $C_{13} = C_{23}$, $C_{44} = C_{55}$, $C_{66} = 0.5(C_{11} - C_{12})$. The effective elastic constants for the polysynthetically-twinned γ-TiAl + α_2-Ti_3Al single crystals are obtained as a proper weighted average.

The evolution equation for the plastic deformation gradient is defined by the flow rule:

$$\dot{F}^p F^{p-1} = \sum_\beta \dot{\gamma}^\alpha S_0^\alpha, \quad S_0^\alpha \equiv m_0^\alpha \otimes n_0^\alpha, \tag{5}$$

where S_0^α is the Schmid tensor and $\otimes$ denotes the tensorial product of the two vectors.

The components of a unit slip plane normal n_0^α and a unit slip direction m_0^α in the reference configurations of the two phases are defined relative to the respective orthonormal bases in the two phases.

The plastic shearing rate $\dot{\gamma}^\alpha$ on a slip system α is described using the following simple power-law relation:

$$\dot{\gamma}^\alpha = \dot{\tilde{\gamma}} \frac{|\tau^\alpha|}{|s^\alpha|}^{1/m} \operatorname{sign}(\tau^\alpha) \tag{6}$$

where $\dot{\tilde{\gamma}}$ is a reference plastic shearing rate, τ^α and s^α are the resolved shear stress and the deformation resistance on slip system α, respectively and m is the material rate-sensitivity parameter.

Since elastic stretches in intermetallic materials is generally small, the resolved shear stress on slip system α can be defined as:

$$\tau^\alpha = T^* \cdot S_0^\alpha \tag{7}$$

where the raised dot denotes the scalar product between two second order tensors.

Finally, the slip system resistance is taken to evolve as:

$$\dot{s}^\alpha = \sum_\beta h^{\alpha\beta} |\dot{\gamma}^\beta| \tag{8}$$

where $h^{\alpha\beta}$ describes the rate of strain hardening on the slip system α due to the shearing on the coplanar (self-hardening) and non-coplanar (latent-hardening) slip systems β and is given the following simple form:

$$h^{\alpha\beta} = q^{\alpha\beta} h^\beta \tag{9}$$

where, h^β denotes the self-hardening rate while $q^{\alpha\beta}$ is a matrix describing the latent hardening behavior for

which the following simple form is adopted:

$$q^{\alpha\beta} = \begin{matrix} 1 \\ q_l \end{matrix} \begin{cases} \text{if } \alpha \text{ and } \beta \text{ are coplanar slip systems,} \\ \text{otherwise} \end{cases} \tag{10}$$

The polysynthetically-twinned γ-TiAl + α_2-Ti_3Al single crystal as modeled by Grujicic and Batchu [13] has one γ-TiAl based set of coplanar slip systems defined as following: $(111)[1\bar{1}0]$, $(111)[10\bar{1}]$, and $(111)[01\bar{1}]$.

The self-hardening rate h^β is defined as:

$$h^\beta = h_0^\beta \left| 1 - \frac{s^\beta}{s_s^\beta} \right|^\tau \operatorname{sign}\left(1 - \frac{s^\beta}{s_s^\beta} \right). \tag{11}$$

where h_0^β is the initial hardening rate and s_s^β the saturation slip deformation resistance and r power exponent.

Finite element analysis of deformation and fracture behavior of polysynthetically-twinned polycrystalline γ-TiAl + α_2-Ti_3Al materials requires the integration of the material state represented by Equations 9, 10 and 12 along the loading path. A detailed description of this procedure and its implementation into a User Material Subroutine (UMAT) of Abaqus/Standard is given in our previous work [23].

2.3. Polycrystalline finite element method

To analyze the deformation and fracture behavior of polycrystalline γ-TiAl + α_2-Ti_3Al materials, a finite element mesh shown in Fig. 4a consisting of 971 quadrilateral and 364 triangular elements is used in the present work. The mesh is partitioned into 27 equiaxed (hexagonal) lamellar colonies, Fig. 4b. The materials constituent response of each of the colonies is described using the crystal-plasticity model of Grujicic and Batchu [13] for polysynthetically twinned γ-TiAl + α_2-Ti_3Al single crystals which was reviewed in the previous section. No provisions are made for the presence of interlamellar boundaries within the colonies. However, colony boundaries are modeled using the cohesive zone approach, which allows boundary decohesion. The initial orientation of colonies 14, 19 and 20 are chosen in such a way that in each of these colonies, the lamellar interfaces are normal to the x–y plane of the finite element mesh, Figure 4(b), and their traces make an angle of 0°, 60° and 120° with the x-axis, respectively. The initial orientation of the remaining colonies, as defined by the appropriate set of three Euler angles, is assigned at random. The initial (reference) configuration is assumed to be stress free and not to contain any lattice perturbations. The polycrystalline aggregates defined in Fig. 4b is loaded in the y direction while constraining the four straight edges of the aggregates to remain straight and parallel to their original orientation with no strain being allowed in z direction. While the aggregate does not possess any special symmetry and, hence, is not expected to deform in the enforced orthotropic manner, the aggregate is considered here as a "material point" and according to the Taylor assumption, the

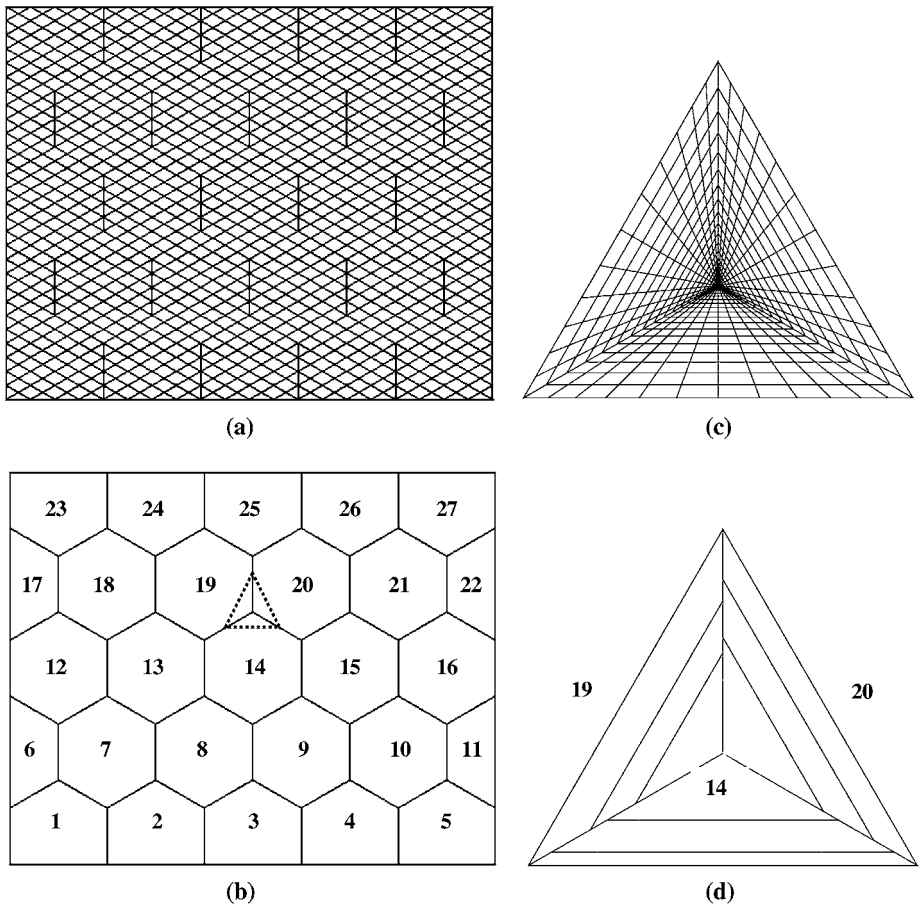

Figure 4 (a) The finite element mesh consisting of 971 quadrilateral and 364 triangular elements; (b) The polycrystalline reference configuration consisting of 27 lamellar colonies; (c) The finite element mesh consisting of 612 quadrilateral and 36 triangular elements, and (d) The polycrystalline reference configuration consisting of three lamellar colonies, each containing two γ-TiAl/γ-TiAl interlamellar boundaries.

deformation gradient of each material point is assumed to be equal to the global deformation gradient.

Based on the results obtained for the polycrystalline aggregate, the triangular region marked using dashed lines in Fig. 4a is selected for a further, fine-scale finite element analysis. This region is divided into 612 quadrilateral and 36 triangular elements, Fig. 4c, and partitioned into three colonies, Fig. 4d. The crystallographic orientation of the material in the three colonies is set to be identical to that of colonies 14, 19 and 20 in Fig. 4b. Each colony boundary is again modeled using the cohesive zone approach. In addition, each colony is allowed to have two γ-TiAl/γ-TiAl lamellar interfaces. The position of the lamellar interfaces within the colonies is chosen at random. The loading on the three-colony aggregate shown in Fig. 4c is applied by setting the displacement history of the boundary nodes of this aggregate to be identical to the deformation history of the corresponding triangular region marked in Fig. 4b.

3. Results and discussion

3.1. Aggregate consisting of 27 γ-TiAl + α_2-Ti_3Al lamellar colonies

In this section, the deformation fields are shown and analyzed for the 27-colony γ-TiAl + α_2-Ti_3Al aggregate, Fig. 4b, loaded in plane-strain tension. Specifically, the contour plots are shown for: (a) the equivalent plastic strain; (b) the angle of the lattice rotation; (c) the hydrostatic stress and; (d) the equivalent stress.

The distributions of the equivalent plastic strain, the lattice-rotation angle, the hydrostatic stress and the equivalent stress for the 27-colony aggregate at the total normal strain in the y-direction of 1.5% are shown in Fig. 5a–d, respectively.

The equivalent plastic strain contour plot shown in Fig. 5a clearly indicates a nonuniform distribution of the equivalent plastic strain. The values of the equivalent plastic strain in Fig. 5a range between 0.05% (the lightest shade of gray) and 2.44% (the darkest shade of gray). Furthermore, localization of the strain into deformation bands inclined relative to the x-axis at an angle of $\approx\pm 40^\circ$, as marked by arrows in Fig. 5a, is apparent. The same deformation bands could be first observed at the total normal strain in the y-direction of $\approx$0.5% (the contour plot not shown for brevity) and as deformation proceeded, they become more pronounced.

In addition to the nonuniformity in the distribution of the equivalent plastic strain on a length-scale of the 27-colony aggregate, the distribution of the equivalent plastic strain is quite nonuniform within each colony as well. For example, within colonies 8, 13, 14, 19, etc., at the total normal strain in the y direction of 1.5%, Fig. 5a, the equivalent plastic strain ranges between 0.2 and 2.44%. Furthermore, some colonies contain regions of high gradients of the equivalent plastic strain. Such regions are often located either near the colony boundaries (e.g. colony boundaries associated with colonies 7 and 12 and colonies 10 and 15) or near

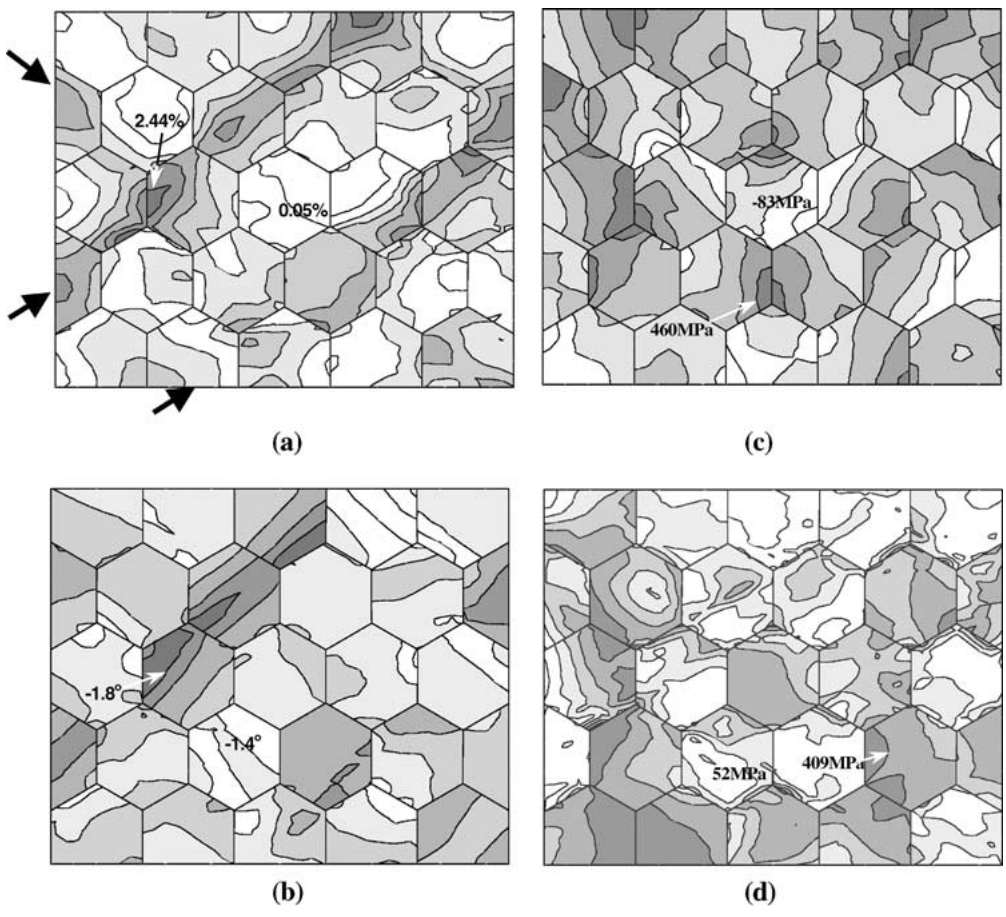

Figure 5 Contour plots in the 27-colony aggregate at the overall noraml strain of 1.5% in the vertical direction (the darker the shade of gray the higher the value of the corresponding quantity): (a) the equivalent plastic strain (0.05–2.44%); (b) the lattice rotation (-1.4–1.8°); (c) the hydrostatic stress (-83–460 MPa) ; and (d) the equivalent stress (52–409 MPa).

the three-colony junctions (e.g. 7-12-13 and 10-15-16 colony junctions).

The distribution of the magnitude of the lattice rotation in the 27-colony aggregate at the overall plastic strain of 1.5% is shown in Fig. 5b. Counterclockwise lattice rotations are described as positive while the clockwise lattice rotations are denoted as negative. The values of the lattice rotations in Fig. 5b range between -1.4 (the lightest shade of gray) and $+1.8$ degrees (the darkest shade of gray). A careful examination of Fig. 5b reveals that the largest rotations take place near the colony boundaries (e.g. the boundaries between colonies 12 and 13, colonies 9 and 10, etc.) and near the three-colony junctions (e.g. 3-4-9, 12-13-18, 19-20-25, etc. three-colony junctions). Furthermore, a comparison of the corresponding results shown in Fig. 5a and b suggests that the largest rotations take place within the colonies located in the deformation bands (e.g. colonies 5,13,19 and 20 in one deformation band, and colonies 9 and 22 in another deformation band). This is not surprising since the lattice rotations are the natural consequence of the effect of the orthogonal kinematic constraints imposed by the boundary conditions (e.g. the four straight edges of the 27-colony aggregate are required to remain straight and parallel to their original orientation) and the constraints associated with the surrounding colonies on the crystallographic shear within each colony. Hence, the regions characterized by largest levels of the equivalent plastic strain are generally expected to experience largest magnitudes in the lattice rotation.

The distribution of the hydrostatic stress in the 27-colony aggregate at the overall plastic strain of 1.5% is shown in Fig. 5c. The values of the hydrostatic stress shown in Fig. 5c range between -83 (the lightest shade of gray) and 460 MPa (the darkest shade of gray). This figure clearly shows that the hydrostatic stress is distributed quite nonuniformly not only among the colonies but also within each colony. Some colonies (e.g. 7, 12 and 23, etc.) are subject to positive (tensile) hydrostatic stresses, while the others (e.g. 14, 19, 20, etc.) experience both positive (tensile) and negative (compressive) hydrostatic stresses. High-magnitude hydrostatic stresses are generally concentrated near the colony boundaries or near the three-colony junctions. In particular, the three-colony junctions associated with colonies 7, 12 and 13 and colonies 14, 19, and 20 are characterized by a high gradient and a large magnitude of the positive hydrostatic stress. A comparison of the results shown in Fig. 5c with the results shown in Fig. 5a and b suggests that the most probable cause for the observed high magnitude and high gradient of the hydrostatic stress at the 7-12-13 three-colony junction is the incompatibility of the plastic deformation in the three colonies which is manifested by a large variation in the equivalent plastic strain and in the lattice rotations across the 7-13 and 12-13 colony boundaries. On the other hand, since neither the equivalent plastic strain nor the lattice rotations vary greatly in the region surrounding the 14-19-20 three-colony junction, the concentration of the hydrostatic stresses in this case, appears to be associated with the elastic anisotropy and pronounced misorientation of the crystal lattice in the three joining colonies.

The distribution of the equivalent stress in the 27-colony aggregate at the overall plastic strain of 1.5% is shown in Fig. 5d. The values of the equivalent stress shown in Fig. 5d range between 52 (the lightest shade of gray) and 409 MPa (the darkest shade of gray). This figure clearly shows that the distribution of the equivalent stress is quite nonuniform both on a length-scale of the 27-colony aggregate as well as on the length-scale of a single colony. By comparing the results in Fig. 5d with the results shown in Fig. 5a and b, no clear correlation between the distributions of the equivalent plastic strain and the lattice rotations on one hand and the equivalent stress on the other can be established. Similar comparison of the results shown in Fig. 5d with the results shown in Fig. 5c, however, suggests that the regions of a high concentration of the hydrostatic stress (e.g. 7-12-13 and 14-19-20 three-colony junctions) are generally associated with high gradients in the equivalent stress. Furthermore, in many cases, several closed equivalent-stress contours could be seen within a single colony (e.g. colonies 8, 18, 19, etc.). The presence of such contours is a clear indication of the kinematic constraints imposed by the surrounding colonies on the given colony.

The equivalent plastic-strain, the lattice rotation angle, the hydrostatic stress and the equivalent stress contour plots in the 27-colony aggregate at the total normal strain in the y direction of 3.0% are shown in Fig. 6a–d, respectively. Nonuniform distribution of the above-mentioned quantities, which was observed and analyzed at the total normal strain in the y-direction of 1.5%, is retained and even somewhat more pronounced. For instance, the shear bands seen in Fig. 6a are sharper than the corresponding ones observed in Fig. 5a. The equivalent plastic strain shown in Fig. 6a ranges between 0.06 and 5.57% in comparison to the 0.05 to 2.44% equivalent plastic strain range associated with Fig. 5a. Similar observations can be made by comparing the contour plots in Fig. 6b–d with the corresponding ones displayed in Fig. 5b–d. The range of the respective quantities (the angle of the lattice rotation, the hydrostatic stress, and the equivalent stress) are given respectively in the captions of Fig. 6b–d.

At this point it is worth noting that the observed distributions in hydrostatic and equivalent stresses, equivalent plastic strains and lattice rotations at the overall plastic strains of 1.5% and 3.0%, Figs 5a–d and 6a–d, are quite similar to their counterparts reported by Asaro and co-workers [7, 11]. This finding is reasonable since at these levels of the overall plastic strain, the extent of decohesion along colony boundaries (modeled in the present work but not in the work of Asaro and co-workers [7, 11]) is quite limited.

At the overall strain of 3.19%, pronounced decohesion occurred along the 14-19 and 14-20 colony-boundaries causing the execution of the Abaqus/Standard job to terminate. With the exception of the hydrostatic stress, the equivalent plastic strain, the lattice rotation and the equivalent stress contour plots at the total normal strain in the y-direction of

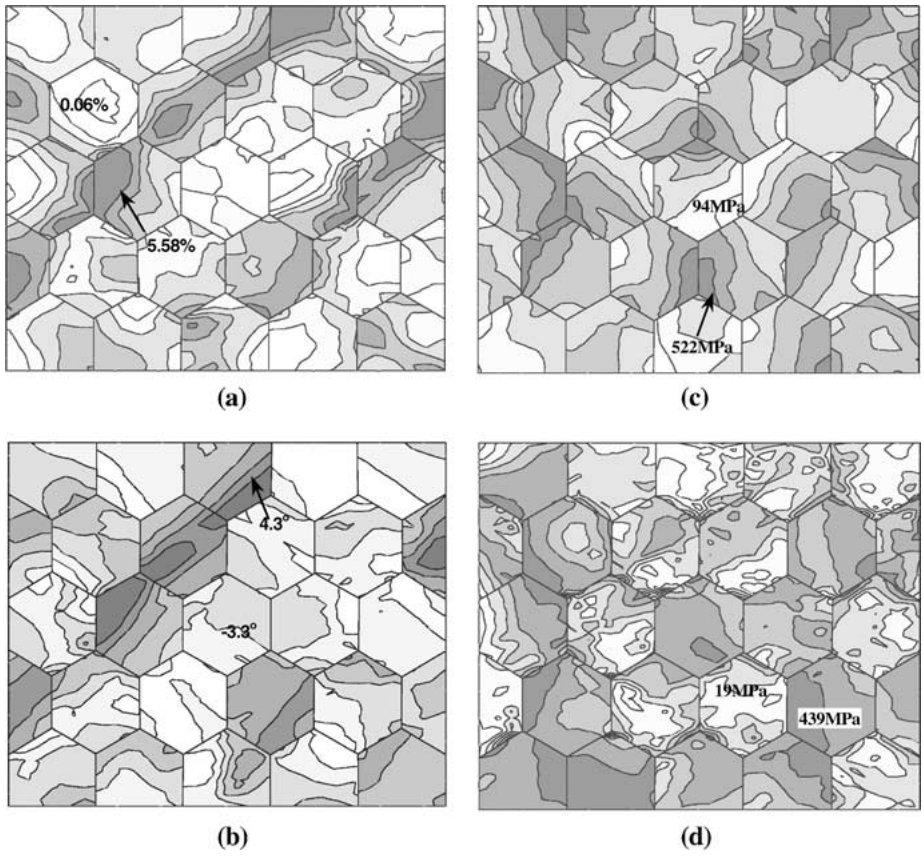

Figure 6 Contour plots in the 27-colony aggregate at the overall noraml strain of 3.0% in the vertical direction (the darker the shade of gray the higher the value of the corresponding quantity): (a) the quivalent plastic strain (0.06–5.58%); (b) the lattice rotation (−3.3–4.3°); (c) the hydrostatic stress (94–522 MPa); and (d) the equivalent stress (19–439 MPa).

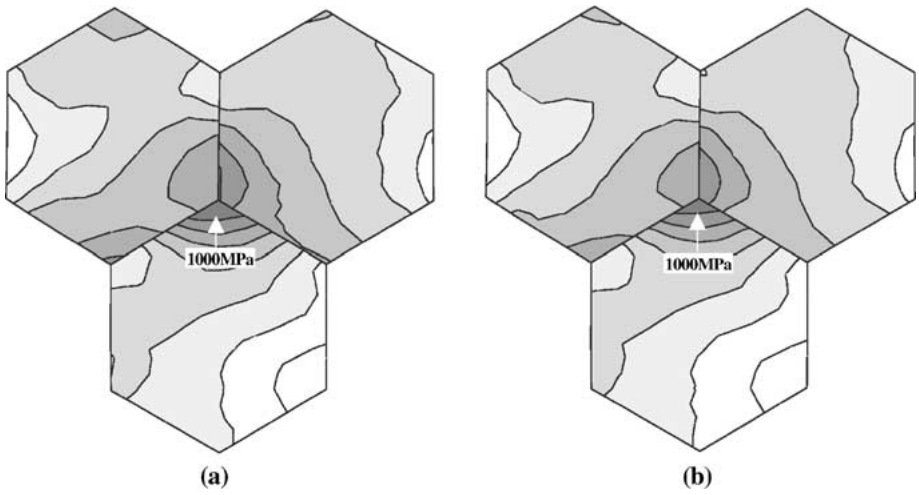

Figure 7 The hydrostatic stress contour plots in colonies 14, 19 and 20 of the 27-colony aggregate at the overall noraml strains in the vertical direction of: (a) 3.0% and (b) 3.19%. To assist comapisonof, the contour lines in (a) and (b) are are placed at the same levels of the hydrostaic stress.

3.19% are very similar to the ones at 3% of the same type of strain, Fig. 6a and b and d. Hence these contour plots are not shown. As far as the hydrostatic stress is concerned, it undergoes a significant change in the range of the total normal strain in the y direction between 3.0 and 3.19 only in the vicinity of the 14-19-20 three-colony junction. Hence, in Fig. 7a–b, contour plots for the hydrostatic stress are shown only for the region comprising colonies 14, 19 and 20. To assist comparison of the results shown in Fig. 7a and b, the contour lines are placed at the same levels of the hydrostatic stress in the two figures. As evident from the results shown in Fig. 7a and b, the hydrostatic stress decreases as loading is proceeded between the total normal strain in the y direction of 3.0% and 3.19%. As mentioned earlier, this is caused by decohesion which takes place along the 14-19 and 14-20 colony boundaries. The decohesion process along the 14-19 and 14-20 colony-boundaries and its relationship with the presence of lamellae in the three colonies is examined in more details in the next section.

3.2. Aggregate consisting of three γ-TiAl + α_2-Ti_3Al lamellar colonies

In order to better understand the conditions leading to material fracture by decohesion along colony boundaries and the effect of lamellar interfaces within the colonies on the strain to fracture, a finite element

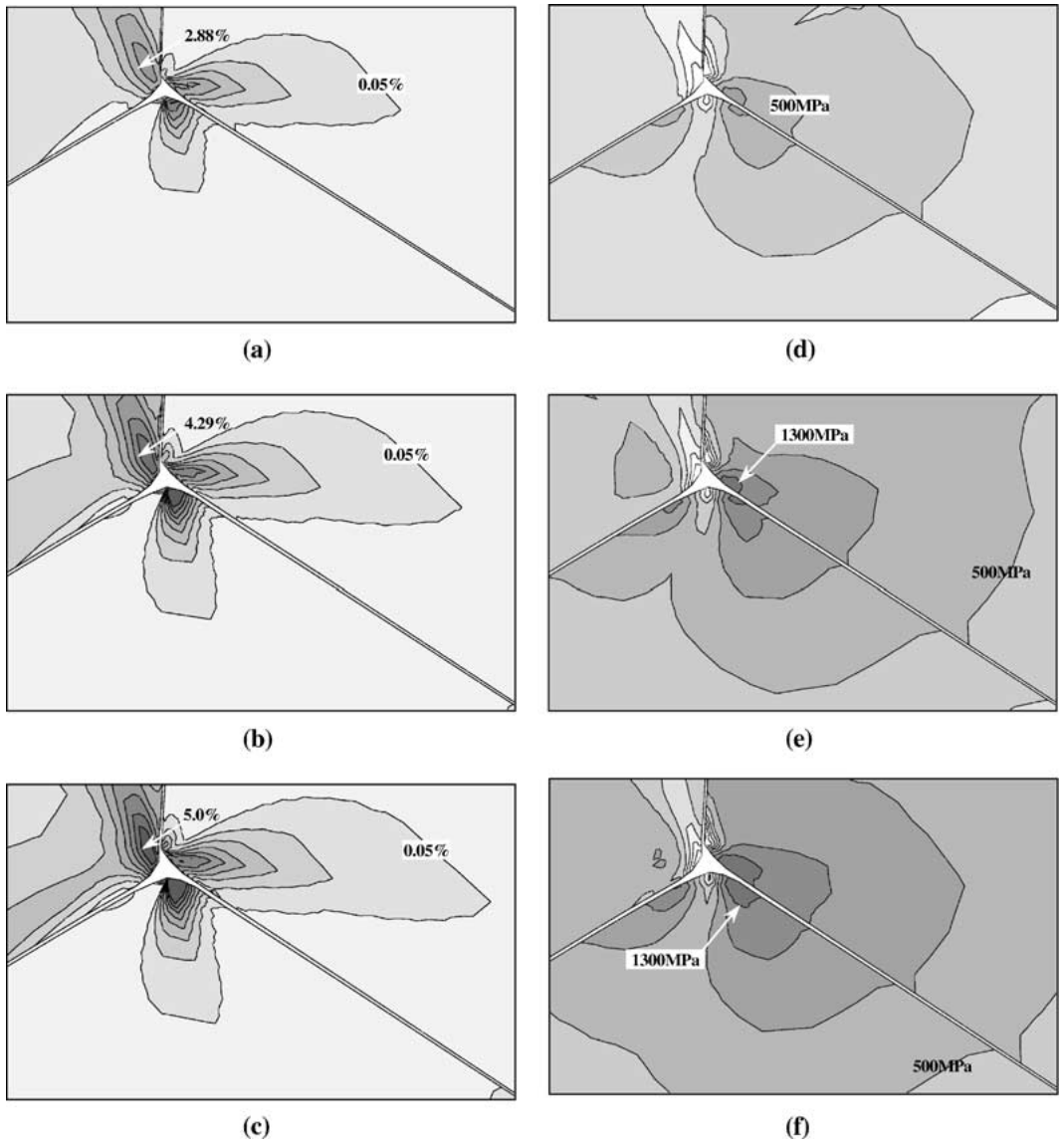

Figure 8 Contour plots for the equivalent plastic strain, (a)–(c), and the hydrostatic stress, (d)–(f) in a region surrounding the three-colony junction of the 3-colony aggregate without lamellar interfaces at the overall noraml strain: (a) and (d) 2.5%; (b) and (e) 3.0% and (c) and (f) 3.19%. The two quantitis vary between 0.05% and 500 MPa (the lightest shade of gray) and 5.0% and 1300 MPa (the darkest shade of gray), respectively.

analysis of the evolution and the distributions of the deformation fields discussed in the previous section, at a smaller length scale, the length scale of the triangular region surrounding the 14-19-20 three-colony junction is carried out in this section. As discussed in Section 2.3, external loading of this region is achieved by prescribing the displacements along its external boundaries. The evolution of these displacements during loading is set to be identical to that for the corresponding triangular region in the 27-colony aggregate, Fig. 4b.

The distributions of the equivalent plastic strain and the hydrostatic stress in the triangular 3-colony aggregate without lamellar interfaces at the total normal strain in the y-direction of 2.5, 3.0 and 3.19% are shown in Fig. 8a–f, respectively. For improved clarity only the innermost rectangular region surrounding the 14-19-20 three-colony junction is shown in these figures. The results shown in Fig. 8a–f can be summarized as follows:

- In accordance with the equivalent plastic strain distribution results at the length-scale of the 27-colony aggregate, Figs 5a and 6a, the level of the equivalent plastic strain in colony 19 is considerably higher than those in colonies 14 and 20 when viewed at the length-scale of the 3-colony aggregate, Fig. 8a–c. This finding suggests that the loading applied to the 3-colony aggregate is consistent with the loading experienced by the corresponding triangular region in the 27-colony aggregate, Fig. 4b.
- While some of the equivalent plastic strain contours located within colony 19, Fig. 8a–c, are generally aligned with the $+40^\circ$ deformation band, Figs 5a and 6a, the equivalent plastic strain distribution near the three-colony junction is dominated by incompatibilities in plastic deformation of the adjoining colonies and colony-boundaries decohesion.
- Even at an overall normal strain in the y direction of 2.5%, prominent 14-19 and 14-20 colony-boundary decohesion is observed. However, at this level of the overall normal strain in the y direction, decohesion is localized to a small region surrounding the 14-19-20 three-colony junction. As

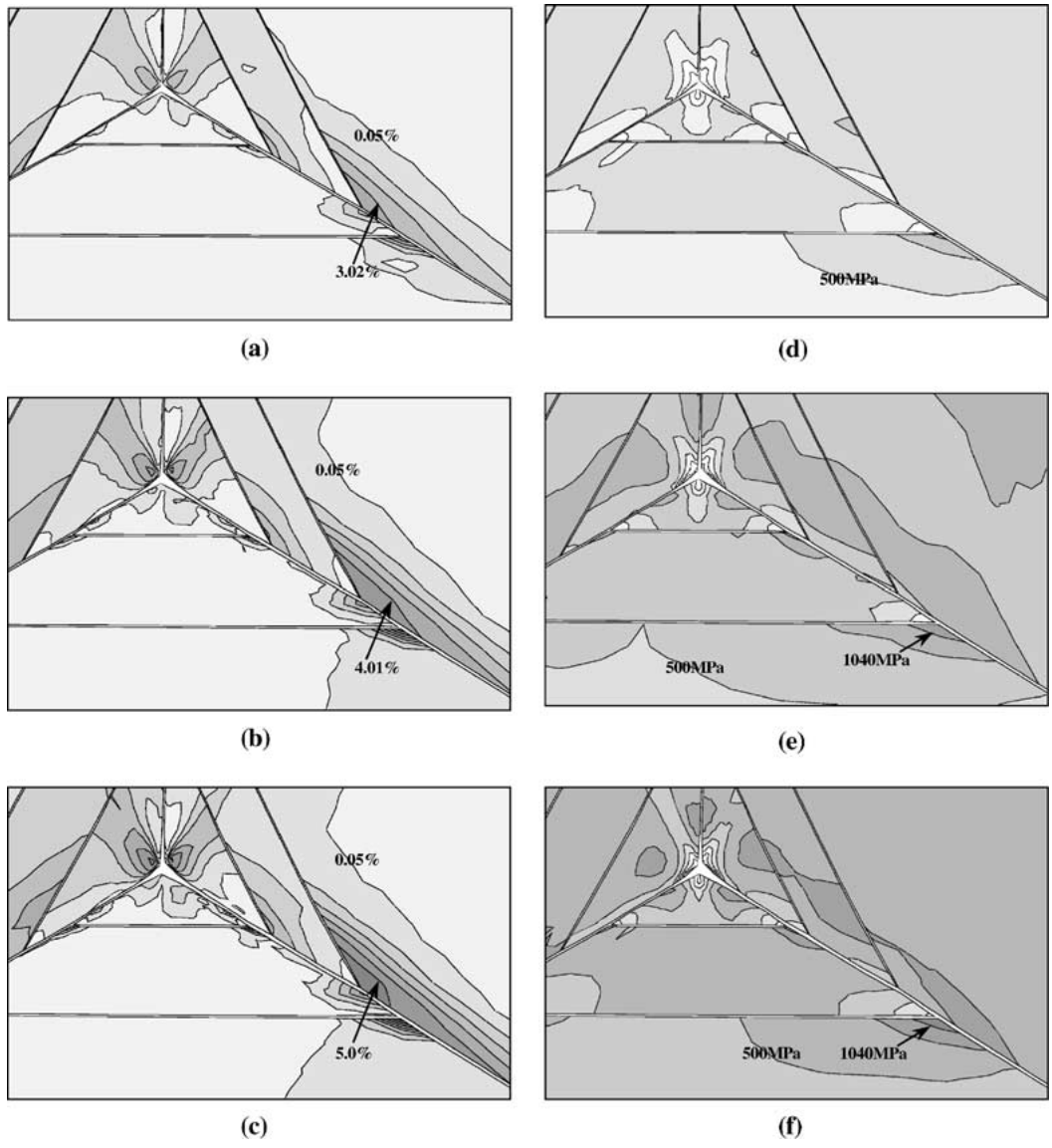

Figure 9 Contour plots for the equivalent plastic strain, (a)–(c), and the hydrostatic stress, (d)–(f) in a region surrounding the three-colony junction of the 3-colony aggregate with two lamellar interfaces per colony at the overall normal strain: (a) and (d) 2.5%; (b) and (e) 3.0% and (c) and (f) 3.19%. The two quantities vary between 0.05% and 500 MPa (the lightest shade of gray) and 5.0% and 1300 MPa (the darkest shade of gray), respectively.

loading is continued, on the other hand, decohesion extends along the two colony-boundaries. It should be noted that in order to improve the clarity of the results, displacements in Fig. 8a–f are magnified by a factor of 50.

– The progression of decohesion is closely related to the distribution of the hydrostatic stress, Fig. 8d–f. That is, as loading is continued, the hydrostatic stress increases, causing an increase in the normal displacement jump across colony boundaries. However, once displacement jumps exceed a critical value, (which is dependent on the magnitudes of the corresponding colony-boundary shear displacement jumps) the boundary's ability to support the load decreases and local (decohesion-induced) unloading takes place. Some evidence of such unloading can be seen by comparing the hydrostatic stress contours in Fig. 8e and f.
– The distributions of the equivalent plastic strain and the hydrostatic stress in the triangular 3-colony aggregate in which each colony contains two lamellar interfaces at the total normal strain in the y-direction of 2.5, 3.0 and 3.19% are shown in Fig. 9a–f, respectively. To enable a comparison with the results shown in Fig. 8a–f, the same rectangular region surrounding the 14-19-20 three-colony junction is shown in Fig. 9a–f. In addition, same levels of the equivalent plastic strain/hydrostatic stress are represented in the two sets of figures using the same shades of gray. The results shown in Fig. 9a–f can be summarized as follows:
– As in the case of the 3-colony aggregate without interlamellar boundaries, Fig. 8a–c, the equivalent plastic strain is also localized near the 14-19-20 three-colony junction in the present case, Fig. 9a–c. However, significant localization of the equivalent plastic strain near intersections of the colony boundaries and lamellar interfaces can also be observed.
– At the identical levels of the overall normal strain in the y direction, the extent of decohesion along colony boundaries in the material containing interlamellar boundaries, Fig. 9a–f, is significantly

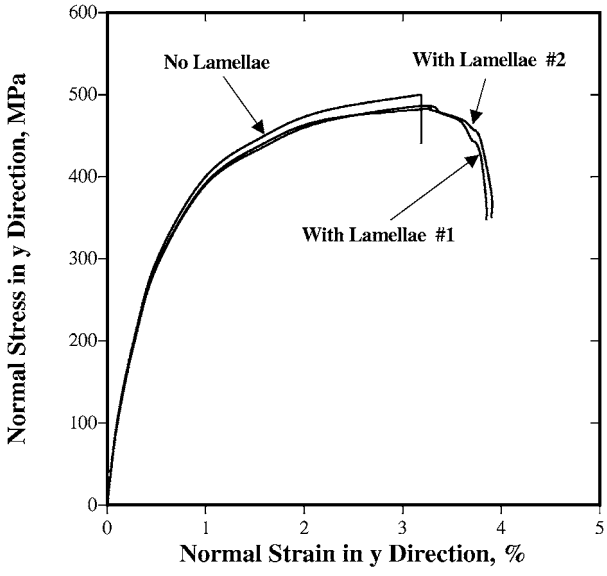

Figure 10 Normal stress versus normal strain in the y direction in a 3-colony aggregate without interlamellar boundaries ("No Lamellae") and in two 3-colony aggregates with interlamellar boundaries ("With Lamellae #1" and "With Lamelae #2").

lower than in the material without lamellar interfaces, Fig. 8a–f. However, in the former case, considerable decohesion takes place also along interlamellar boundaries.

– In comparison with the results shown in Fig. 8d–f, the hydrostatic-stress contour plots for the material with interlamellar boundaries, Fig. 9d–f, show that hydrostatic stress is lower in magnitude and more uniformly distributed. This finding suggests that the presence of lamellar interfaces facilitates accommodation of the incompatibilities in plastic flow of the adjacent colonies. In addition, the results shown in Fig. 9d–f indicate that relatively high hydrostatic stresses are situated not only near the 14-19-20 three-colony junction but also near the colony-boundary/lamellar-interface intersections.

The average normal stress versus normal strain (in the y direction) curves for the 3-colony aggregates without and with interlamellar boundaries are shown in Fig. 10. The curve denoted as "No Lamellae" corresponds to the 3-colony aggregate without lamellar interfaces and shows that in this case the material undergoes an abrupt fracture at the overall normal strain of 3.19%. Contrary, in the 3-colony aggregates containing lamellar interfaces (Curves labeled "With Lamellae #1" and "With Lamellae #2", fracture is somewhat delayed (fracture strain 3.8–3.9%) and occurs in a more gradual manner. The curve labeled "With Lamellae #1" corresponds to the 3-colony aggregate for which the contour plots are displayed in Fig. 9a–f. The curve labeled "With Lamellae #2", on the other hand, corresponds to another 3-colony aggregate (not shown for brevity) with a different location of lamellar interfaces. The second 3-colony aggregate with lamellar interfaces is used to confirm that the observed effects of increased strain to fracture and a more gradual nature of the fracture process are primary due to the presence of lamellar interfaces and not due to their fortuitous location in the first 3-colony aggregate.

4. Conclusions

Based on the results obtained in the present study the following main conclusions can be drawn:

– The incompatibilities in plastic flow between the adjacent lamellar colonies in polycrystalline γ-TiAl + α_2-Ti_3Al materials resulting from a pronounced plastic anisotropy in these materials can give rise to a large build-up of the tensile hydrostatic stress in regions surrounding certain three-colony junctions and, in turn, can lead to material fracture via colony-boundary decohesion.
– The fracture behavior of the material following the onset of colony-boundary decohesion appears to be greatly affected by the absence/presence of interlamellar boundaries. In the absence of interlamellar boundaries, decohesion along colony-boundaries continues to take place quite rapidly leading to imminent fracture of the material. In sharp contrast, when interlamellar boundaries are present, they also undergo some decohesion. Consequently, instead of decohesion taking place rapidly and solely along colony boundaries, it also spreads out to adjacent lamellar interfaces. As a result, fracture occurs in a more gradual manner and the material becomes more damage resistant.
– The tensile fracture strains (3–4%), predicted in the present work are very comparable to experimental counterparts [e.g., 19] suggesting that colony-boundary decohesion plays a critical role in fracture of the materials at hand. This observation is consistent with the scanning electron microscopy results of Kad *et al*. [7], which showed that while the fracture surface reveals a combination of the intercolony (along colony boundaries) and transcolony (along interlamellar boundaries) fracture modes, the region underneath the fracture surface contains numerous colony-boundary cracks. In other words, the fracture appears to be initiated and, most likely controlled, by colony boundary decohesion.
– The presence of interlamellar boundaries is found to improve materials tensile ductility, which is fully consistent with the experimental observations of Grujicic and Dang [19] that lamellar γ-TiAl-base intermetallics posses higher strain to fracture than their single-phase (non-lamellar) counterparts.

Appendix A: Derivation of the interface elements stiffness matrix

The γ-TiAl/γ-TiAl lamellar interface and colony boundary potentials developed in Section 2.1 are incorporated into the UEL subroutine of Abaqus/Standard to compute the stiffness matrix of the corresponding interfacial elements. The UEL subroutine allows the user to define the contribution of interfacial elements to the global finite element model. In other words, for the given nodal displacements of the interface elements provided to UEL by Abaqus/Standard, the contribution of the interfacial elements to the global vector of residual forces and to the global Jacobian (element stiffness matrix) is determined in the UEL subroutine and

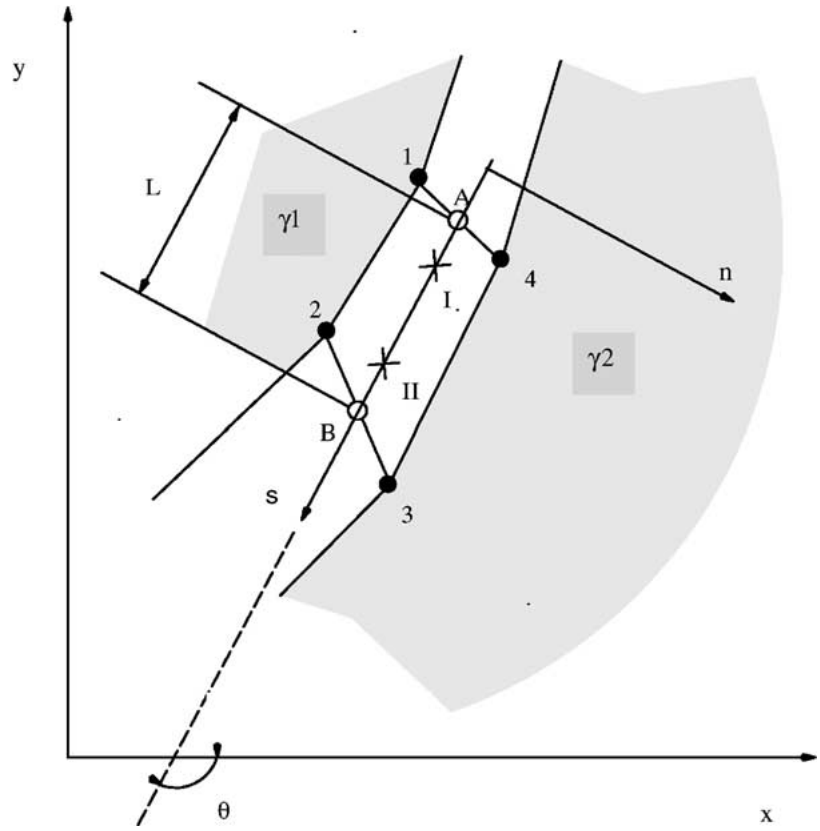

Figure A1 Definition of a linear, four-node interface element. Nodes 1 and 4 and nodes 2 and 3 coincide in the reference configuration. Internal nodes A and B located at the midpoints of segments connecting corresponding nodes on the opposite sides of the interface, two integration points marked as + and a local s-n coordinate system are also indicated.

passed to Abaqus/Standard. The implementation of the γ-TiAl/γ-TiAl interface/boundary potentials (derived in Section 2.1) in the UEL subroutine is discussed below.

Since only two-dimensional analysis is carried out in the present work, each interface element is defined as a four-node isoparametric element on the γ-TiAl/γ-TiAl lamellar interface/colony boundary S, as shown schematically in Fig. A1. In the undeformed configuration (not shown for brevity), nodes 1 and 4, and nodes 2 and 3 coincide, respectively. A local coordinate system, consistent with the directions, which are tangent (s) and normal (n) to the interface, is next assigned to the each element. Direction s is colinear with directions t and b used in Section 2.1 so that $U_t = U_s \cos\alpha$ and $U_b = U_s \sin\alpha$ where U_t, U_b and U_s are displacements along the three tangential directions and α is the angle between s and t shear directions. Next, two 'internal nodes', A and B, located at the midpoints of the lines 1-2 and 3-4, connecting the corresponding interface/boundary nodes of the two lamellae/colonies are introduced. The interface displacements at the internal nodes A and B are expressed in terms of the displacements of the element nodes 1–4 as:

$$U_n^A = \left(U_y^4 - U_y^1\right)\cos\theta - \left(U_x^4 - U_x^1\right)\sin\theta \quad \text{(A1)}$$

$$U_s^A = \left(U_y^4 - U_y^1\right)\cos\theta - \left(U_x^4 - U_x^1\right)\sin\theta \quad \text{(A2)}$$

$$U_n^B = \left(U_y^3 - U_y^2\right)\cos\theta - \left(U_x^3 - U_x^2\right)\sin\theta \quad \text{(A3)}$$

$$U_s^A = \left(U_y^4 - U_y^1\right)\cos\theta - \left(U_x^4 - U_x^1\right)\sin\theta \quad \text{(A4)}$$

An isoparametric coordinate η is next introduced along the tangent direction with $\eta(A) = -1$ and $\eta(B) = 1$ and two linear Langrangian interpolation functions are defined as $N_A(\eta) = (1-\eta)/2$ and $N_B(\eta) = (1+\eta)/2$.

The interpolation functions given above allow the normal and the tangential components of the interface displacements to be expressed in the form of their values at the internal nodes A and B as:

$$U_s(\eta) = N_A(\eta)U_s^A + N_B(\eta)U_s^B \quad \text{(A5)}$$

$$U_n(\eta) = N_A(\eta)U_n^A + N_B(\eta)U_n^B \quad \text{(A6)}$$

The tangential and normal components of the forces at nodes A and B, i.e. F_s^A, F_s^B, F_n^A and F_n^B, which are work conjugates of the corresponding nodal displacements U_s^A, U_s^B, U_n^A and U_n^B are next determined through the application of the virtual work to the interfacial element as:

$$\int_{-1}^{1} \delta\Phi(\eta) L\pi r(\eta)\,\mathrm{d}\eta = \sum_{I=n.s}\sum_{N=A.B} F_I^N \delta U_I^N \quad \text{(A7)}$$

where L is the A-B element length. The perturbation of interface potential is expressed in terms of the perturbations of the interface displacements at the internal nodes A and B, U_s^A, U_s^B, U_n^A and U_n^B as:

$$\partial\Phi = \frac{\partial\Phi[U_s(\eta), U_n(\eta)]}{\partial U_n}\left[N_A(\eta)\delta U_n^A + N_B(\eta)\delta U_n^B\right] + \frac{\partial\phi[U_s(\eta), U_n(\eta)]}{\partial U_s}\left[N_A(\eta)\delta U_s^A + N_B(\eta)\delta U_s^B\right] \quad \text{(A8)}$$

By substituting Equation A8 into A7 and by choosing one of the δU_I^N $(N = A, B; l = s, n)$ perturbations at a time to be unity and the remaining perturbations to be zero, the corresponding F_I^N component of the nodal force can be expressed as:

$$F_I^N = \int_{-1}^{1} \frac{\partial \Phi[U_s(\eta), U_n(\eta)]}{\partial U_I} N_N(\eta) L \pi r(\eta)\, \mathrm{d}\eta \quad \text{(A9)}$$

Using a straightforward geometrical procedure and imposing the equilibrium condition, the corresponding residual nodal forces R_x^i and R_y^i $(i = 1\text{–}4)$ in the global x-y coordinate system, are defined as:

$$\begin{aligned} R_x^1 &= -R_x^4 = F_s^A \cos\theta - F_n^A \sin\theta \\ R_y^1 &= -R_y^4 = F_s^A \sin\theta - F_n^A \cos\theta \\ R_x^2 &= -R_x^3 = F_s^B \cos\theta - F_n^B \sin\theta \\ R_y^2 &= -R_y^3 = F_s^B \sin\theta - F_n^B \cos\theta \end{aligned} \quad \text{(A10)}$$

The components of the element Jacobian are next defined as:

$$\frac{\partial R_j^i}{\partial U_I^k} = \sum_{I=n\cdot s} \sum_{N=A\cdot B} \sum_{j=n\cdot s} \sum_{M=A\cdot B} \frac{\partial R_j^i}{\partial F_I^N} \frac{\partial F_I^N}{\partial U_J^M} \frac{\partial U_J^M}{\partial U_I^k} \quad \text{(A11)}$$

where the components of the internal Jacobian $\frac{\partial F_I^N}{\partial U_J^M}$ $(i, j = n, t; N, M = A, B)$ are calculated by differentiation of Equation A9. The residual nodal forces given by Equation A10 and the element Jacobian given by Equation A11 are computed in the UEL subroutine, and passed to Abaqus/Standard for accurate assessment of kinematics in its global Newton scheme.

Acknowledgements

The material presented here is based on work supported by the National Science Foundation, Grant Numbers DMR-9906268 and CMS-9531930 and by the U.S. Army Grant Number DAAH04-96-1-0197. The authors are indebted to Dr. K. L. Murty of NSF and Dr. David M. Stepp of ARO for the continuing interest in the present work. The authors also acknowledge the support of the Office of High Performance Computing Facilities at Clemson University.

References

1. M. YAMAGUCHI and Y. UMAKOSHI, *Prog. Mater. Sci.* **34** (1990) 1.
2. L. A. JOHNSON, D. P. POPE and J. O. STIEGLER (eds.), High-temperature Ordered Intermetallic Alloys IV, Materials Research Society Symposium Proceedings, Pittsburgh, Pennsylvania, Vol. 213, 1991.
3. S. H. WHANG, C. T. LIU, D. P. POPE and J. O. STIEGLER (eds.), "High-temperature Aluminides and Intermetallics," The Minerals, Metals and Materials Society, Warrendale, PA, 1990.
4. T. FUJIWARA, A. M. NAKAMURA, M. HOSOMI, S. R. NISHITANI, Y. SHIRAI and M. YAMAGUCHI, *Phil. Mag.* A **61** (1990) 591.
5. Y. W. KIM, *Acta Metall. Mater.* **40** (1992) 1121.
6. T. NAKANO, A. YOKOYAMA and Y. UMAKOSHI, *Scripta Metall.* **27** (1992) 1253.
7. B. K. KAD, M. DAO and R. J. ASARO, *Phil. Mag.* A **71** (1995) 567.
8. "Abaqus/Standard 5.8 User Manual" (Hibbit, Karlsson & Sorenson, Inc., Providence, R.I., 1998).
9. C. TEODOSIU and F. SIDOROFF, *International Journal of Engineering Science* **14** (1976) 165.
10. R. J. ASARO and J. R. RICE, *Journal of the Mechanics and Physics of Solids* **25** (1977) 309.
11. M. DAO, B. K. KAD and R. J. ASARO, *Phil. Mag.* A **74** (1996) 569.
12. B. J. LEE, B. K. KAD and R. J. ASARO, *Scripta Metall* **29** (1993) 823.
13. M. GRUJICIC and S. BATCHU, *J. Mater. Sci.* **36** (2001) 2581.
14. A. NEEDELMAN, *J. Appl. Mech.* **54** (1987) 525.
15. M. GRUJICIC and S. G. LAI, *J. Mater. Sci.* **33** (1998) 4385.
16. M. S. DAW and M. I. BASKES, *Phys. Rev. Lett.* **50** (1983) 1285.
17. *Idem.*, *Phys. Rev.* B **29** (1984) 6443.
18. D. FARKAS, private communication.
19. M. GRUJICIC and P. DANG, *Mater. Sci. Engng.* A **224** (1997) 187.
20. *Idem.*, *J. Mater. Sci.* **32** (1997) 4875.
21. M. GRUJICIC and S. G. LAI, *ibid.* **33** (1998) 4401.
22. M. GRUJICIC and Y. ZHANG, *ibid.* A **265** (1999) 285.
23. *Idem.*, *ibid.* **34** (1999) 1419.
24. R. FLETCHER and C. M. REEVES, *Comput. J.* **7** (1964) 149.
25. P. VILLARS and L. O. CALVERT, "Pearson's Handbook of Crystallographic Data for Intermetallic Phases," Vol. 2 (American Society for Metals, Metals Park, OH, 1985).
26. S. SOCRATE, Ph.D. thesis, MIT, Cambridge, MA, 1996.
27. G. BOZZOLO, I. FARRANTE and J. R. SMITH, *Scripta Metall.* **25** (1991) 1927.
28. C. TEODOSIU, in Proceedings of the Conference on Fundamental Aspects of Dislocation Theory, edited by R. Simmons, J. A. DeWit and R. Bullough (McMillan, London, 1970) p. 837.
29. R. HILL and J. R. RICE, *Journal of the Mechanics and Physics of Solids* **20** (1972) 401.
30. J. MANDEL, in Proceedings of the International Symposium on Foundations of Continuum Thermodynamics, edited by D. Domingos, J. J. Nina and J. H. Whitlaw (McMillan, London, 1974) p. 283.
31. R. J. ASARO, *ASME Journal of Applied Mechanics* **50** (1983) 921.
32. U. F. KOCKS, A. S. ARGON and M. F. ASHBY, *Progress in Material Science* **19** (1975) 1.
33. H. J. FROST and M. F. ASHBY, "Deformation Mechanism Maps" (Pergamon Press, New York, 1982).
34. A. S. ARGON, in "Physical Metallurgy," edited by R. W. Cahn and P. Haasen (Elsevier, Amsterdam, 1995).
35. H. INUI, Y. TODA and M. YAMAGUCHI, *Phil. Mag.* A **67** (1993) 1315.

Received 4 December 2001
and accepted 18 September 2002